Punching of arbitrary face prismatic loops from hydrogen nanobubbles in copper

Lopez Cazalilla, Alvaro

2022-02-15

Lopez Cazalilla , A , Djurabekova , F , Granberg , F , Mizohata , K , Perez-Fontenla , A T , Calatroni , S & Wuensch , W 2022 , ' Punching of arbitrary face prismatic loops from hydrogen nanobubbles in copper ' , Acta Materialia , vol. 225 , 117554 . https://doi.org/10.1016/j.actamat.2021.11755

http://hdl.handle.net/10138/341720
https://doi.org/10.1016/j.actamat.2021.117554

Acta Materialia 225 (2022) 117554

Contents lists available at ScienceDirect

Acta Materialia

journal homepage: www.elsevier.com/locate/actamat

Full length article

Punching of arbitrary face prismatic loops from hydrogen nanobubbles in copper

A. Lopez-Cazalilla [a,*], F. Djurabekova [a], F. Granberg [a], Kenichiro Mizohata [a], Ana Teresa Perez-Fontenla [b], Sergio Calatroni [b], Walter Wuensch [b]

[a] Department of Physics, University of Helsinki, P.O. Box 43, FI-00014, Finland
[b] CERN, European Organization for Nuclear Research, Geneva 1211, Switzerland

ARTICLE INFO

Article history:
Received 31 July 2021
Revised 27 October 2021
Accepted 8 December 2021
Available online 10 December 2021

Keywords:
Molecular dynamics
Copper
Prismatic loop punching
Bubble growth
Hydrogen

ABSTRACT

When a metal surface is exposed to prolonged irradiation with energetic H^-, the ions are expected to penetrate into bulk and dissolve in the matrix. However, the irradiated surfaces exhibit dramatic morphological changes in the form of "blisters" covering the surface exposed to irradiation. Blistering is usually explained by accumulation of implanted gas in the bubbles near surface. However, the exact mechanism of continuous growth of a bubble after it reaches the measurable size is still not fully clear. Commonly such growth is related to prismatic loop punching, which is a short time scale process not easily accessible by experimental techniques. Even atomistic modelling of loop punching in FCC metals is somewhat cumbersome. Since the void surfaces in these metals yield easily through shear loops, these were debatably suggested to explain the plastic growth of a bubble in copper, without demonstrating the detachment of these loops from the void.

We address the mechanisms of fast bubble growth in Cu which is associated with blistering of Cu surface exposed to H^- irradiation. We observe the emission of a complete prismatic loop enclosed within the number of shear loops with the Burgers vectors aligned with the gliding direction of the prismatic loop. We show that the prismatic loops punched from the bubble surface do not need to be smaller than the bubble cross-section. These simulations capture the general trend of dislocation emission in the condition of hydrostatic pressure exerted by the accumulated gas on the wall of the bubble.

1. Introduction

Blistering is a process of modification of surface morphology of materials that are exposed to prolonged irradiation with energetic ions of hydrogen and inert gases [1]. The lack of chemical bonding and a large mass ratio between the implanted atoms and the atoms of the matrix was observed to lead to the preferential accumulation of the former in different types of sinks such as lattice imperfections, surface, and grain boundaries [2–4]. Vacancies formed in the irradiated matrix by energetic atoms are also able to accommodate more than one implanted light atom [5–7]. Since the light and inert gas atoms bind readily to empty lattice sites, they can induce emission of interstitial atoms, if there is more than one bound gas atom. This process increases the empty volume and more of the implanted atoms may fit in it [8]. This eventually leads to growth, within the metal matrix, of a bubble, i.e. a void filled with the implanted gas, analogous to gas bubbles growing in boiling liquid. It has been shown that the bubbles grow gradually from 1.5 to 2 nm [9] to much larger sizes, which can eventually be seen on the surface of the irradiated metal as "blisters", i.e hillocks filled with the implanted gas [10–14]. Blistering has been studied primarily in tungsten, since it is the most promising candidate for plasma facing materials for future fusion nuclear power plants [8–10,15]. However, the process is not specific to this material only. It has also been observed in many other metals, such as V [16], Nb [17], carbon steel [18–20], Fe [21–23], Al [24–29] and Cu [12–14,30–32]. For instance, proton irradiation of Cu surfaces up to high fluences (1.3×10^{23} H/m^2) showed hydrogen bubbles in Cu already in 1980 [33].

Different mechanisms were identified to explain the gas bubble growth. A bubble can grow not only via pushing interstitials one by one from the place of accumulation of the implanted atoms, but also via vacancy diffusion, agglomeration of vacancies into clus-

* Corresponding author.
E-mail address: alvaro.lopezcazalilla@helsinki.fi (A. Lopez-Cazalilla).

https://doi.org/10.1016/j.actamat.2021.117554

ters and, finally, coalescence of smaller mobile clusters into larger stable ones [1]. For instance, during H irradiation of Cu, the mobile mono-vacancies were seen to trap several H atoms (up to 6) depending on ambient temperature [5]. These mono-vacancies interact with one another forming vacancy clusters, which may still migrate either absorbing more vacancies or coalescing with other vacancy clusters.

The increasing number density of the trapped implanted atoms results in pressurized gas, switching the mechanism of bubble growth from diffusion- to dislocation-mediated through plastic deformations. The latter become possible due to the strong pressure exerted by the trapped gas on the bubble walls. The appearance of blisters on the irradiated material surface cannot be explained by vacancy migration, but by plastic deformation within the surface. However, continuous plastic deformations in metals leads to its hardening, hindering dislocation activity, while blistering is a continuous process: the blisters were seen to grow continuously with increased exposure of metal surfaces to ion beams [13,14,30].

Due to low stacking fault energy, plastic deformations at a bubble surface in an FCC lattice result in emission of Shockley partial dislocations, forming shear loops that expand from the bubble surface. Emission of large number of these loops can indeed lead to dilation of the bubble [34]. However, continuous growth of a bubble can be expected only if there is mass transport of atoms from the bubble surface. Although there were attempts to show that emission of shear loops can also induce mass transport [35,36], the authors were not able to show that these shear loops leave the surface of the void. As argued in [37], the only way to induce the void growth is to punch a prismatic loop. The analytical model describing the process of loop punching correlated the position of their emission with the spots of the highest stress concentration on the void surface [38,39]. Indeed, the prismatic loops were simulated in very small He bubbles in W [40] and Cu [41]. These studies confirm that emission of prismatic loops is possible not only in BCC, which has been successfully studied by atomistic modelling [42–44] but also in FCC structures with extensive slip system which supports nucleation of multiple partial dislocations with perpendicular Burgers vectors. However, it is still not clear whether the same mechanism holds for large bubbles, where emission of multiple dislocations further enhanced by large surface area hinder the collective atom transport away from the bubble surface. However, recently Zhou et al. [44] studied the emission of prismatic loops due to nanoindentation in different materials: Cu, Al and Ni (FCC) and Ta and Fe (BCC). The authors found a distinct difference in prismatic loop formation in both FCC and BCC metals: successive pop-in modes (displacement excursions in the pressure versus displacement curves) more common in FCC metals, whereas in BCC the single pop-in type modes prevail.

In Refs. [45–47], the growth of near-surface voids under tensile stress exerted at the Cu surface by an applied electric field was studied. It was clearly seen that the shear loops growing away from the void surface, eventually left the surface of the void and created atomic steps on the top of the surface. Hence, it was concluded that the prismatic loops were punched from the surface of the void. These, however, were not clearly observed in the simulations, since the size of the shear loops surrounding the prismatic one were extensive, while the distance between the void and the surface was rather short.

In this work, we focus on plastic deformation around the bubble surface in Cu filled with hydrogen gas. Our experiments show that even under relatively low energy H^- ion irradiation of Cu surface, the surface blisters appear after many hours of exposure. The effect causes dramatic changes on the surface affecting its electric field holding properties as well. Using molecular dynamics simulations, we show that pressurized hydrogen gas is able to exert sufficient pressure on the walls of the bubble to induce clear prismatic dislocation loop punching, which is indeed the driving mechanism of hydrogen bubble growth within Cu as it is able to mass transport atoms away from the bubble surface. The shape of the prismatic loops, which we see in the current simulations, is consistent with the shape of protrusions observed in [47] and with the shape of blisters observed in experimental images. This consistency confirms that the mechanism of hydrogen bubble growth in Cu is mediated by the prismatic loop punching, starting from nanometric bubble size.

2. Methods

2.1. Experiment

The experiment aims at studying blistering phenomena which have been observed at the Radio-Frequency Quadrupole (RFQ) of the LHC injector chain at CERN, where stray beam from the H^- source impacts the entrance copper surfaces of the RFQ at an energy of 45 keV to 3 MeV. In our experiments, we used Cu-OFE (oxygen-free electronic-grade copper, UNS C10100) electrodes that were prepared by diamond machining from a multi-directional forged bar [48]. The shapes of electrodes (anode and cathode) were compatible with the large electrode system described in detail in Ref. [49]. The samples were subjected to degreasing after machining, followed by a thermal treatment at 835 °C for 20 min with a 100 °C/h heating ramp, which reproduces the vacuum brazing cycle used in the fabrication of the current RFQ.

Irradiation was performed at CERN by using a spare identical twin of the H^- source that injects into the operational RFQ. The sample was installed in vacuum downstream the source with a fixture allowing beam incidence perpendicular to the sample surface. Beam energy was 45 keV at a fluence of $\sim 2.5 \times 10^{19}$ H^-/cm^2 with an exposure time of 40 hours, and a duty cycle of about 0.1% at a repetition rate of 1 Hz. H^- is fully ionized into H^+ within less than 1 at. diameter after entering the copper surface [50], and calculations show that H^+ at 45 keV has then a Bragg peak at a depth of about 300 nm.

To show the continuous growth dynamics we performed additional experiments using the 500 kV HVE (High Voltage Engineering Europa) ion implanter available in the Accelerator Laboratory of the University of Helsinki. In these experiments, the Cu-OFE surface was irradiated by the 90 keV positively charged H_2^+ molecular DC beam to enable the same energy per atom as in the RFQ experiment. The irradiation was performed by raster scanning the ion beam over the implantation area in horizontal and vertical directions using electrostatic beam deflectors at 10 kHz and 1 kHz, respectively. The Cu-OFE samples were irradiated to two different fluences 4×10^{18} H/cm^2 and 1×10^{18} H/cm^2 through the ring shaped Faraday cup. The ion beam flux was maintained below 1×10^{14} $H/cm^2/s$ during both irradiation procedures, while the exposure times were 18 h and 4.5 h, respectively.

Blisters on the sample were imaged by using a Scanning Electron Microscope (SEM) model Sigma from Zeiss.

2.2. Molecular dynamics simulations

2.2.1. Interatomic potentials

All simulations were performed by using the PARCAS MD code [51]. The Cu-Cu interactions are described by the embedded atom model (EAM) interatomic potential developed by Mishin et al.[52] (hereafter, *Mishin* potential), to describe accurately mechanical properties of copper. Following the approach used in [53,54], we also describe the H-H interactions in the EAM formalism using the potential developed for the Ni-Al-H system [55]. The potential predicts formation of H_2 molecules with the bond length $d_{H-H} =$ 0.75Å and the bond energy $E_{H-H} = 4.74$ eV. We verified that the

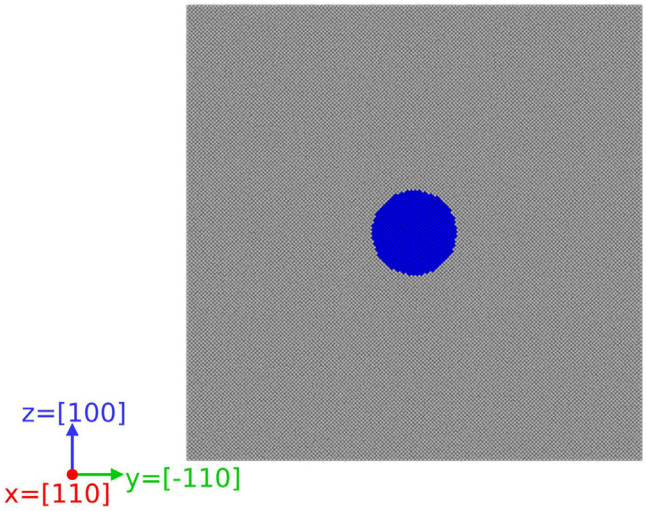

Fig. 1. Initial configuration of the simulation cell with dimensions $42 \times 42 \times 42$ nm^3. A 4 nm radius void is positioned in the center of the cell and shown in blue. (For interpretation of the references to colour in this figure legend, the reader is referred to the web version of this article.)

behavior of the pressurized H gas follows that of the gaseous phase and exerts hydrostatic pressure on the walls of the bubble. Additionally, we simulated a He bubble in Cu, where He-He interactions were described by the ZBL potential [56] to avoid organization of gas atoms into a lattice. The response of Cu lattice was very similar, see Fig. B1(a–f) in Supplementary material B, confirming that the bubble surface yields under hydrostatic gas pressure within the bubble and not because of possible effects of the pressurized H.

The Cu-H interactions in our simulations were described by the purely repulsive ZBL potential [56], which also allows us focusing on effects of the gas pressure in the bubble, rather than on chemical interactions of gas atoms with the lattice and possible escape of H atoms into the lattice. The latter assumption is reasonable due to low solubility limit of H in Cu [57].

We were not able to benefit from the existence of the bond-order potential (BOP) proposed in Ref. [58]. Although this potential describes all interactions needed for the current study (Cu-Cu, H-Cu and H-H), its inefficiency and poor description of processes under high gas pressures within the bubble limited the application of this potential in our simulations.

2.2.2. Simulation setup

The simulation cell $42 \times 42 \times 42$ nm^3 (6233910 Cu atoms) in size was initially relaxed at 600 K and zero pressure by applying Berendsen thermo- and barostats [59] with the periodic boundary conditions in all directions.

We introduced the bubble into the simulation cell by cutting out a spherical void of 4 nm in radius (remaining in the cell 6,212,454 Cu atoms) in the center of the cell and filling it with H atoms of different concentrations. We note that the amount of H atoms included in the simulated bubbles may have resulted in higher gas pressures than those that are expected to trigger the bubble growth in experiment. Keeping in mind the stochastic nature of this process [60,61], much longer experimental times may allow emission of dislocation from a bubble surface at lower pressures. In [39], it was analytically estimated that a 10 nm void can yield at $7.2\sigma_y$, where σ_y is the macroscopic yield strength. For Cu, this value amounts to $\approx$ 0.5 GPa, assuming $\sigma_y \approx 70$ MPa [62–64]. The gas pressure in our bubbles is higher to ensure emission and relaxation of dislocations within the 100 ps of the simulated time (starting from approximately 6 GPa or 60 kbar).

The analysis of the pressures exerted by hydrogen gas on the walls of the bubble can be found in Supplementary material A. In Fig. A1(a) we plot the pressure values in kbar obtained in the simulations of the pure H gas with the atomic densities matching those in the bubble simulations with every value of the hydrogen concentration ($n_{H/vac}$) as a function of $n_{H/vac}$. The H gas was relaxed in NVT for 100 ps at 600 K. We also verified the applicability limit of the used potential [55] by compressing the cell with the highest atomic density ($n_{H/vac} = 5$) in NPT. The results are shown in Fig. A1 (b). We saw that the temperature rapidly rising and atom mobility rapidly decreasing, which indicates formation of a new phase, only at the pressure above 8000 kbar (see the black dashed vertical line in Fig. A1 (b)). The highest pressure used in the current simulation was an order of magnitude below this ultimate limit of the potential applicability.

The orientation of the cell and positioning of the bubble are shown in Fig. 1.

For visualization of the results, we use the Open Visualization Tool (OVITO) [65]. We analyzed the stacking faults in the cells by using the centrosymmetry (CS) parameter [66] and the dislocation extraction algorithm (DXA) available in OVITO [67].

2.2.3. Simulation of a hydrogen bubble

In this work, we ignore the initial stages of the bubble growth and focus on plastic deformations leading to continuous growth of a pre-existing bubble. We study the effect of hydrogen pressure by varying the gas concentration. For every missing Cu atom (a vacancy, "vac") within the void, we introduce a certain number of H atoms ($n_{H/vac}$, number of H per Cu vacancy), randomly locating them within the void at the distance not closer than 0.9 Å from one another to avoid collapse of the atoms.

Since the binding energy of H to a monovacancy is rather high ($E^b_{H-vac_{Cu}} = 0.4$ eV [5]), we expect that at least one hydrogen atom per missing Cu atom will always be found in the bubbles. However, it has been shown that a vacancy in Cu can bind more than one hydrogen atom [7]. Hence, to create sufficient pressure within the bubble, we fit different numbers of H atoms per vacancy $n_{H/vac} = 0$, 0.8, 1, 1.5, 2, 2.5, 3, 3.5, 4, and 5 within the void. We refer to this quantity as the hydrogen concentration within the bubble to distinguish it from the bubble hydrogen density, which is the number of H atoms per unit volume, $\rho_H = N_H/V_{bubble}$. V_{bubble} is calculated by using the *Construct surface mesh* in OVITO [68]. The obtained volume is approximated to have a spherical shape, which was used to deduce the radius that is compared to the radius of the original void with no hydrogen inside. The difference between two radii Δr was used to estimate the dilation of the bubble under the hydrogen pressure inside.

We also note that the solubility of H in Cu, at T = 600 K and P = 20 kbar (2 GPa), is 69 ppm [57], which also supports the assumption of strong accumulation of H atoms in the bubbles during the prolonged H^- irradiation of Cu surface.

3. Results and discussion

3.1. Blistering on Cu surface under prolonged H^- ion irradiation

Fig. 2 shows the Cu surface exposed to the H^- ion irradiation for 40 hours reaching the fluence of $\sim 2.5 \times 10^{19}$ cm^{-2}. The image clearly shows formation of blisters with either rounded shape or having lids of random, but geometrically well defined shapes, in some cases showing signs of an opening at their apex, probably after having burst open. In some places, the blisters are self-organized in rows along specific crystallographic directions. These features indicate that the dislocation-mediated mechanism, whose linear nature, may explain the geometrically recognizable forms and alignment of the bubbles in a self-organized manner.

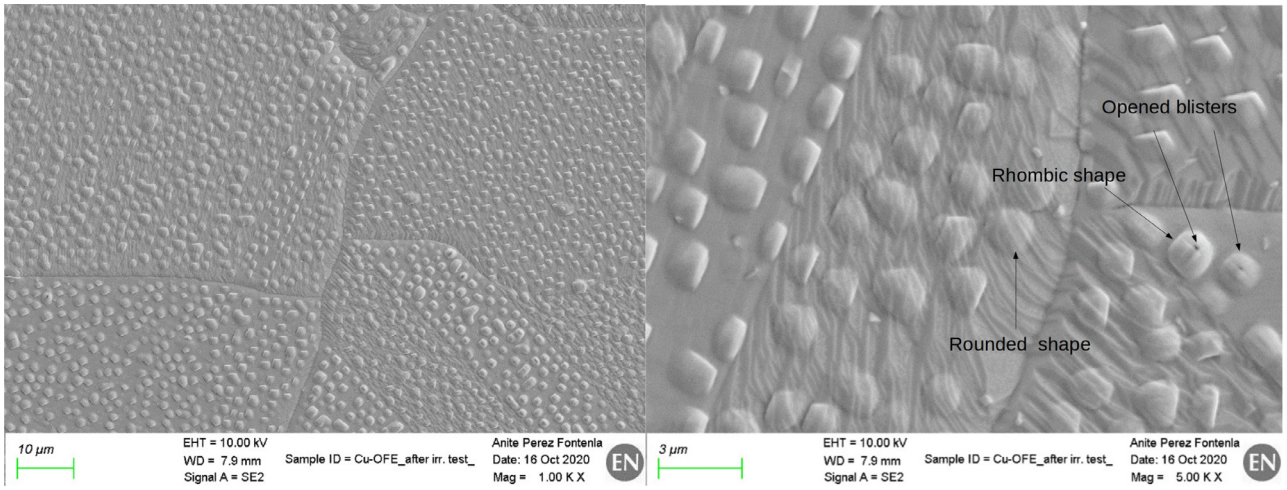

(a) (b)

Fig. 2. SEM images of the Cu surface irradiated by H^- ions up to a fluence of $\sim 2.5 \times 10^{19}$ H^-/cm^2. Imaging was performed with Field Emission Gun Scanning Electron Microscope (FEG-SEM) Sigma (from ZEISS) using the secondary electron detector at 10 keV and various magnifications. The images represent two different locations, with two different levels of magnification.

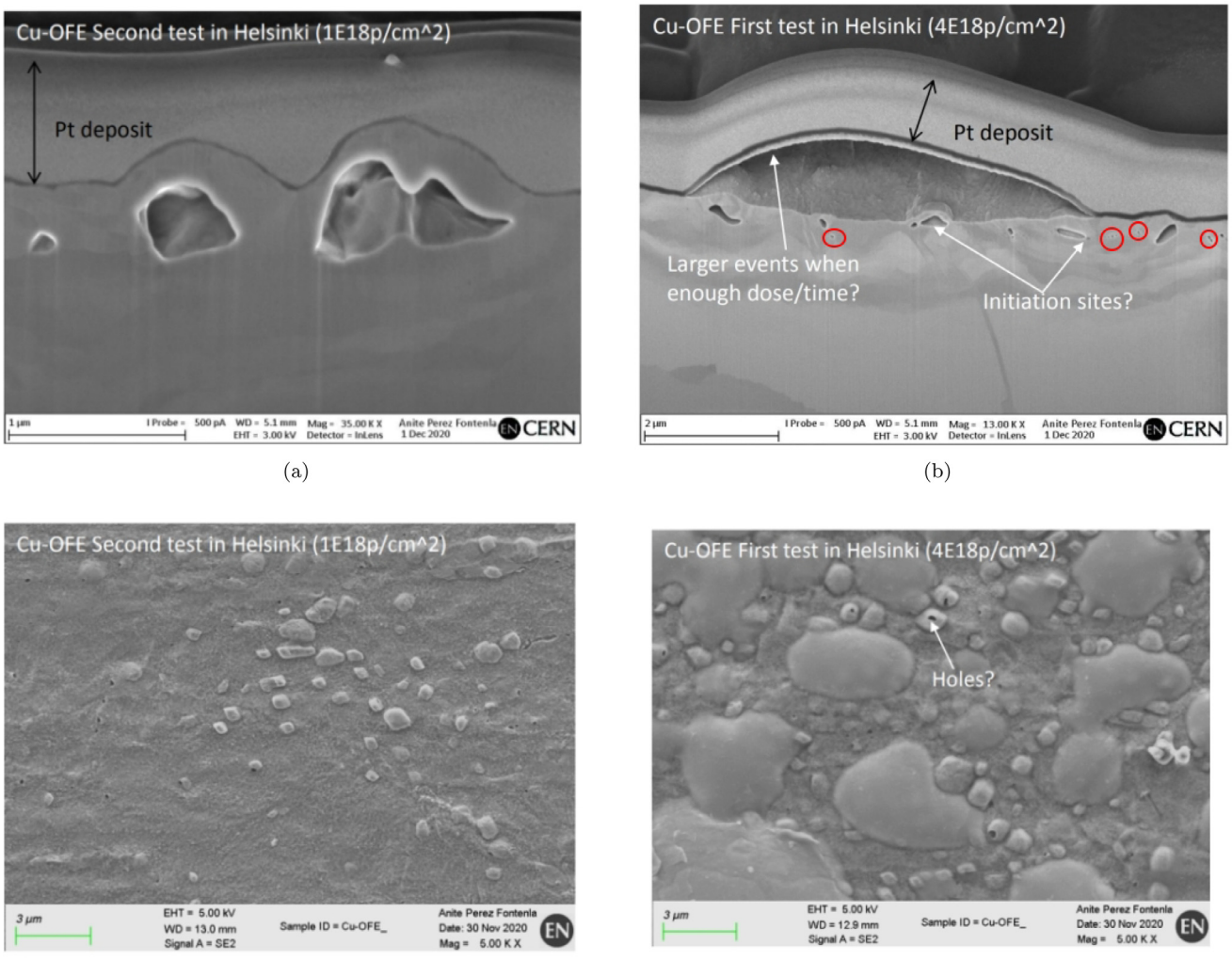

(a) (b)

(c) (d)

Fig. 3. Evolution of OFE-Cu sample under H^+. The cross-section views (a,b) and the top views (c,d) of the surfaces irradiated to fluences of 1×10^{18} cm^{-2}(a,c) and 4×10^{18} cm^{-2} (b,d). The small voids of a few tens of nanometer size are outlined in red. Note that their location is much deeper than the size of the void, which decouples the bubble nucleation process from the effect of the nearby surface. (For interpretation of the references to colour in this figure legend, the reader is referred to the web version of this article.)

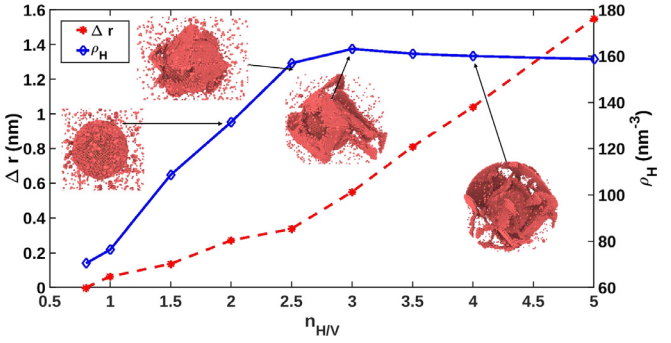

Fig. 4. Evolution of the void radius (red dashed line) and H density inside the void (blue solid line). Inset: intermediate state of the void at 30 ps for $n_{H/vac}$ = 2, 2.5, 3 and 4, respectively from left to right (only those atoms with CS greater than 4.5 and within a sphere of 110 Å of radius are represented). (For interpretation of the references to colour in this figure legend, the reader is referred to the web version of this article.)

The observed geometric shapes of the blisters on Cu surface suggest that the growth of bubbles in Cu must proceed via emission of extended defects rather than individual atoms. In the following, we focus on details of plastic deformation in a hydrogen bubble containing different concentrations of hydrogen. Although the simulations are performed for hydrostatic pressures within the bubble deep in the bulk, the conclusions derived from the study will shed the light on mechanisms developing near bubble surfaces which grow close the surface of the material.

In Fig. 3 we show the bubble growth dynamics under the copper surface which was exposed to the positive H ion beam for extensive times. Fig. 3(a and b) shows the cross sectional view of the bubble structures at (a) the lower (1×10^{18} cm^{-2}) fluence and (b) four times higher fluence (4×10^{18} cm^{-2}). The images in Fig. 3(c and d) shows the top view of the surfaces irradiated to the corresponding fluences as in (a) and (b), respectively. The continuous growth of the bubbles is seen not only in the size of the large blisters, but also in appearance of the new bubbles outlined in the Fig. 3(b) by the red circles and estimated to have size of a few tens of nanometers. These also appear at the depth much larger than the size of the bubble.

Motivated by these experimental observations, we focus in the following on understanding of atom-level mechanisms to explain the hydrogen bubble growth in Cu when the size of the bubble reaches $\sim$ 10 nm in diameter. This is the range of sizes which are already much larger than the initial bubble nuclei (below 2 nm [41]) and may exhibit a different growth dynamics. Moreover, the bubbles can nucleate at the depth exceeding the size of the bubble, see outlined bubbles in Fig. 3(b), whose growth can be decoupled from the presence of nearby surface.

3.2. Bubble size growth under hydrogen gas pressure

In Fig. 4, we show the results of MD simulations indicating the growth of the bubble size as a function of hydrogen concentration ($n_{H/vac}$) within the bubble. The change in the bubble radius Δr (left y-axis) is the difference between the initial radius of the void before filling in the gas and after the structure was filled with gas and fully relaxed in the NPT ensemble for 100 ps. The right y-axis shows the bubble hydrogen density ρ_H. The atomic configurations in the insets of Fig. 4 show evolution of dislocation network around the bubble with increase of the number of H atoms in it. For clarity of illustration we selected only the $n_{H/vac}$values that resulted in plastic deformations around the bubble that are significantly different from the preceding $n_{H/vac}$values. For the corresponding values of the pressure within the bubble exerted by the hydrogen atoms, see Fig. A1 (a) of Supplementary material A. In this graph, the red dashed lines highlight the $n_{H/vac}$value which resulted in the pressure of 20 kbar [57] in our simulations, while the blue dashed lines indicate the pressure (at about $n_{H/vac}$ = 2.5) which resulted in plastic deformation within our MD simulations. This pressure is only three times as high as 20 kbar.

Within 100 ps of the simulated time, the bubble surface did not yield in our simulations until $n_{H/vac}$ = 2.5; correspondingly in this regime, we observed only elastic dilation of the bubble, i.e. both the Δr and ρ_H in Fig. 4 increase linearly. After that, the growth rate of ρ_H suddenly decreases, while the growth rate of Δr increases. This dramatic change marks the start of dislocation emission processes from the surface of the bubble. Indeed the inset with the atomic configuration of the bubble with $n_{H/vac}$ = 2.5 demonstrates formation of a number of stacking faults around the bubble. These stacking faults continue growing and eventually may complete a full stacking fault octahedron. We have previously shown that once such a stacking fault octahedron is formed, the bubble surface becomes more resistant to the gas pressure within the bubble [34]. In the current simulations, we have not observed formation of a complete octahedron, however, even a partially completed one strengthened the bubble surface, so that the hydrogen density still increased (as it is seen in Fig. 4 at about $n_{H/vac}$ = 3).

For $n_{H/vac} \geq$ 3, the hydrogen density within the relaxed bubble does not grow any longer, but on contrary, slightly reduces as the temporary hardening of the surface was removed (the octahedron is no longer seen) and ρ_H reaches the equilibrium value, which is maintained in the bubble despite the increase of hydrogen concentration $n_{H/vac}$. Further growth of $n_{H/vac}$leads to a rapid increase of the bubble size.

We note that the rapid and consistent growth the bubble size can only be explained by activation of a dislocation loop punching mechanism. In the simulations with high $n_{H/vac}$values we see how the bubble initially blows up under the hydrogen pressure inside, but then, the size recovers nearly to the original size, emitting a dislocation from the bubble surface. The videos showing the dislocation evolution dynamics with different $n_{H/vac}$can be seen in Supplementary material C: *n3disloc.mp4, n4disloc.mp4 and n5disloc.mp4*).

The results presented in Fig. 4 can be summarized as follows:

- $n_{H/vac} \leq$ 2.5: Neither dislocation nor any other remarkable defect were detected at the bubble surface. The bubble growth can be described as elastic dilation. Both the change of the bubble radius (red dashed curve) and the bubble hydrogen density (blue solid curve) increase linearly.
- $n_{H/vac} \in$ [2.5,3]: Appearance of stacking faults tangential to the bubble surface, including formation of a full or partial stacking fault octahedron [34] that hardens the bubble surface, which allows for higher bubble hydrogen density. The bubble grows through elastic expansion and plastic deformations via emission of shear loops.
- $n_{H/vac} >$ 3: Octahedron shape around the bubble disappears. The density ρ_H slightly decreases and remain almost at the same value, while the bubble size start rapidly increasing. Hence, a mechanism of mass transport of atoms away from the bubble surface must be activated at this point.

In the following we analyze in detail the mechanisms of plastic deformations around the bubble filled with the H atoms.

3.3. Mechanisms of hydrogen bubble in Cu

Since we observed no significant modification in the cell with $n_{H/vac} <$ 2.5, we discuss the results obtained with the bubble hydrogen concentration corresponding to at least three H atoms per a Cu vacancy.

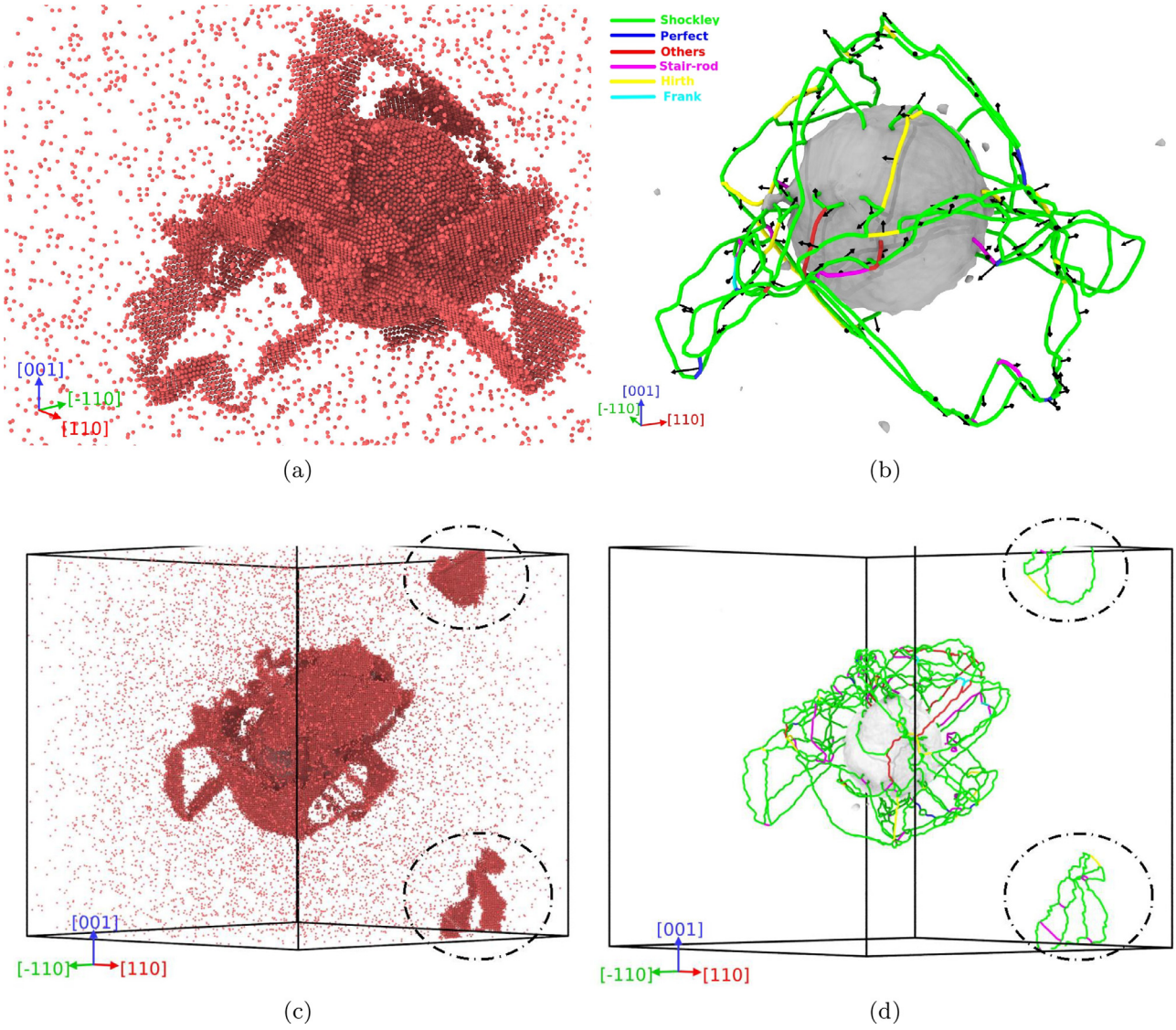

Fig. 5. Dislocations emitted from the bubble with $n_{H/vac} = 3$, (a) and (b), and with $n_{H/vac} = 4$, (c) and (d). In (a) and (c) only the atoms with the CS ≥ 4.5 are shown for clarity, while (b) and (d) show the dislocation lines identified by DXA [67]. The Shockley partials are shown in green, perfect dislocations in blue, undefined dislocations are marked red. The stair-rods are shown in pink, while Hirth and Frank partial dislocations are shown in yellow and cyan, respectively. Dashed lines outline the dislocation loops detached from the surface of the void. (For interpretation of the references to colour in this figure legend, the reader is referred to the web version of this article.)

In Fig. 5, we show the evolution of the Cu structure under the H gas pressure exerted on the walls of the bubble in the middle of the cell. In the left panel, (a) and (c), we visualize only the atoms with the CS parameters ≥ 4.5. In the right panel, (b) and (d), we show the cells with the dislocations identified by the DXA analysis of OVITO. (The nature and quantitative analysis of the dislocations, formed in the cells with $n_{H/vac} = 3$, 4 and 5 can be found in Table C1 of Supplementary material C.)

Stacking faults appeared at the surfaces of the bubble in both cases with $n_{H/vac} = 3$ and $n_{H/vac} = 4$ almost immediately after the simulation has started. The emission of dislocations from the bubble surface clearly provides a mechanism for more significant bubble growth accompanied with a slight release of the bubble gas pressure compared to elastic dilation. Unfortunately, the analysis of the dislocations in the current simulation conditions is not trivial due to high pressure and elevated temperature. However, we can follow the emission of initial dislocations and the general trend of development of dislocation network.

It has been previously shown that the gas trapped within a bubble in an FCC lattice may lead to formation of a stable stacking fault octahedron enveloping the bubble and hardening its surface [34]. Indeed in Fig. 5(a and b), we see a tendency towards the growth of an octahedron in the simulations with $n_{H/vac} = 3$. We have slightly reduced the hydrogen concentration in the bubble and performed addition simulations with $n_{H/vac} = 2.75$, which resulted in the fuller octahedron around the bubble. The results of this simulation can be seen in see Fig. D1(a-d) in Supplementary material D and videos *n2p75-CSP-gt-4p5.mp4* and *n2p75disloc.mp4*. This result suggests that emission of trailing partial dislocations at lower pressure is delayed sufficiently, and the stacking faults on adjacent {111} planes survive longer, which allows to complete the octahedron more readily.

Formation of a stacking fault octahedron around a bubble is specific for FCC lattices because of the extensive slip system. Intuitively one can expect that an octahedron will appear if partial dislocations emit at similar times along all eight {1 1 1} planes tangentially to the bubble surface. Instead, we observed that a slip in one of them, e.g. (1 1 1) in [1 1 0] direction triggers the slip in the adjacent $[1\,\bar{1}\,0]$ direction, promoting the emission of the leading Shockley partial dislocation in this direction on the

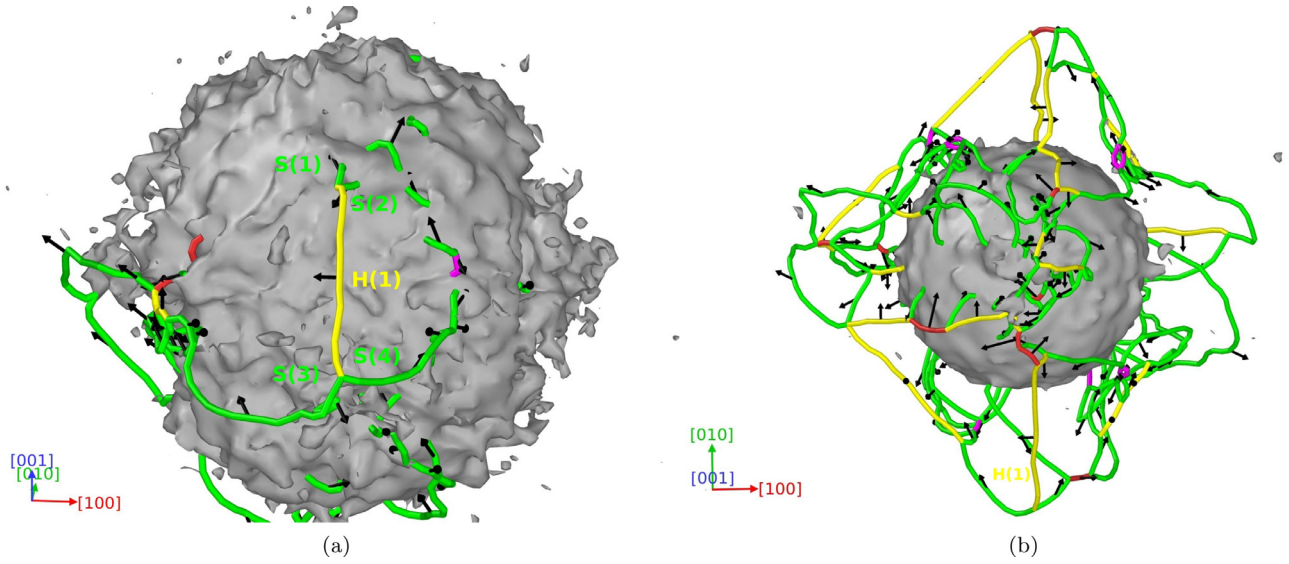

Fig. 6. Hirth dislocations formed around the bubble with $n_{H/vac} = 3$. (a) shows that an initial Hirth lock (**H(1)**) has formed already after 7.5 ps that can build the backbone of the future stacking fault octahedron and (b) shows the top view of the dislocation network evolution after 40 ps, which shows nearly perfect square outlining laterally the forming octahedron. The dislocation lines identified by DXA [67] are shown in different colors according to the dislocation type. The following colors were used: green for Shockley partials, blue for perfect dislocations, red for "others" dislocations, pink for stair-rod, yellow for Hirth and cyan shows Frank partial dislocations. The Burgers vectors of the dislocations are shown. We identify the following dislocations: **H(1)** with $\vec{b} = \frac{1}{3}[\bar{1}00]$, **S(1)** with $\vec{b} = \frac{1}{6}[1\bar{2}\bar{1}]$, **S(2)** with $\vec{b} = \frac{1}{6}[\bar{1}\bar{2}\bar{1}]$, **S(3)** with $\vec{b} = \frac{1}{6}[\bar{1}21]$ and **S(4)** with $\vec{b} = \frac{1}{6}[121]$. The $\langle 100 \rangle$ directions are shown for clarity. (For interpretation of the references to colour in this figure legend, the reader is referred to the web version of this article.)

$(1\,\bar{1}\,\bar{1})$ plane (see movie in Supplementary material *n3rot-disloc-HCP.mp4*)). These two stacking faults grow together vertically along the Hirth lock, which is shown in yellow and marked **H(1)** in the more detailed view in Fig. 6(a).

We notice that although the length of **H(1)** dislocation varies, it remains in the same location almost until the end of the simulation. In previous works [69,70], the formations of a Hirth dislocation were found to follow the dissociation reactions, which can be written, for instance, as:

1:	$\frac{a}{2}[\bar{1}10] + \frac{a}{2}[\bar{1}\bar{1}0] \longrightarrow \frac{a}{6}[\bar{2}1\bar{1}] + \frac{a}{6}[\bar{2}\bar{1}1] + \frac{a}{3}[\bar{1}00]$
2:	$\frac{a}{6}[1\bar{1}2] + \frac{a}{6}[\bar{1}\bar{1}\bar{2}] \longrightarrow \frac{a}{3}[0\bar{1}0]$

where the reaction (**1**) results in two Shockley and one Hirth dislocation and the reaction (**2**) results in a Hirth partial.

In the condition of our simulations, we were not able to trace the entire process of formation of the Hirth dislocation (e.g., **H(1)** in Fig. 6(a) had already appeared at the very beginning of the simulation). The analysis of the Burgers vectors of the dislocations marked in Fig. 6(a) as **H(1)** and **S(1 – 4)** we conclude that **H(1)** is the Hirth partial dislocation with $\vec{b} = \frac{a}{3}[\bar{1}00]$), while the Shockley partials have the following Burgers vectors $\vec{b} = \frac{a}{6}[1\bar{2}\bar{1}]$ (**S(1)**), $\vec{b} = \frac{a}{6}[\bar{1}\bar{2}\bar{1}]$ (**S(2)**), $\vec{b} = \frac{a}{6}[\bar{1}21]$ (**S(3)**) and $\vec{b} = \frac{a}{6}[121]$ (**S(4)**). All of the Shockley partials are leading ones which react to form the Hirth partial as follows:

$$\mathbf{S(2)} + \mathbf{S(3)} = \frac{a}{6}[\bar{1}\bar{2}\bar{1}] + \frac{a}{6}[\bar{1}21] \longrightarrow \frac{a}{3}[\bar{1}00]$$
$$\mathbf{S(1)} + \mathbf{S(4)} = \frac{a}{6}[1\bar{2}\bar{1}] + \frac{a}{6}[121] \longrightarrow \frac{a}{3}[100]$$

Since **S(1)** and **S(3)** as well as **S(4)** and **S(2)** describe the same stacking faults, the Hirth partial is detected in Fig. 6(a) as a single Hirth partial dislocation **H(1)** with the Burgers vector $\vec{b} = \frac{a}{3}[\bar{1}00]$.

Fig. 6(b) shows the top view of the dislocation network around the bubble at a later stage (after 40 ps), when it was fully developed. We can see the almost perfect square which outlines laterally the forming octahedron, although not all sides are fully complete. Moreover, while rotating the image, it can be seen that not all dislocations belong to a geometrically perfect octahedron, some of them are on parallel slip planes further obstructing completion of the perfect octahedron.

In Fig. 7(a), we are able to identify the stacking faults almost in all sides of the octahedron around the bubble (outlined in red). We note that all stacking faults are positioned with some offset from the bubble surface, where the atoms are better organized into the lattice structure. In Fig. 7(c), the same areas are outlined by the dislocations determined by DXA that delimit the stacking faults. The planes correspond to (from left to right) $(\bar{1}\,\bar{1}\,1)$, $(1\,\bar{1}\,1)$ and (1 1 1). One more stacking fault that is not visible from the perspective of the image is on the $(\bar{1}\,\bar{1}\,\bar{1})$ plane (bottom side of the bubble). If these stacking faults grow larger they will be able to complete the full octahedron. The size of the bubble in our simulations does not maintain continuous growth of stacking faults to the sizeable area to complete the full octahedron. In the current scenario, we observe emission of the trailing Shockley partials under the pressure in the bubble before the octahedron is stabilized. However, already partially grown octahedron hardens the material around the bubble surface allowing for more hydrogen pressure to build up within the bubble, see Fig. 4 between $n_{H/vac} = 2.5$ and $n_{H/vac} = 3$. Hence, we anticipate that formation of a full stacking fault octahedron around a bubble may affect the growth dynamics at the earlier growth stage (when the radius $r \lesssim 2$ nm).

The emission of the trailing partials completes the shear loops as shown in Fig. 7 in blue. However, it is also clear that the loops remain attached to the bubble. Fig. 7(a) and 7(b) shows the same instant in the simulations as Fig. 7(c) and 7(d), but from the [1 0 1] direction. Although the shear loops in Fig. 7(a) appear to be connected randomly, from the [1 0 1] directions we can see that they all lie on {111} planes and have the parallel Burgers vectors. Moreover, from this direction it is clear that the emitted shear loops are connected and partially outline a loop perpendicular to themselves. Since this loop is not complete, it remains attached to the bubble until the end of the simulation. It is also worth noting that the loop is slightly larger than the size of the bubble, which is somewhat surprising, since the prismatic loops were always associated

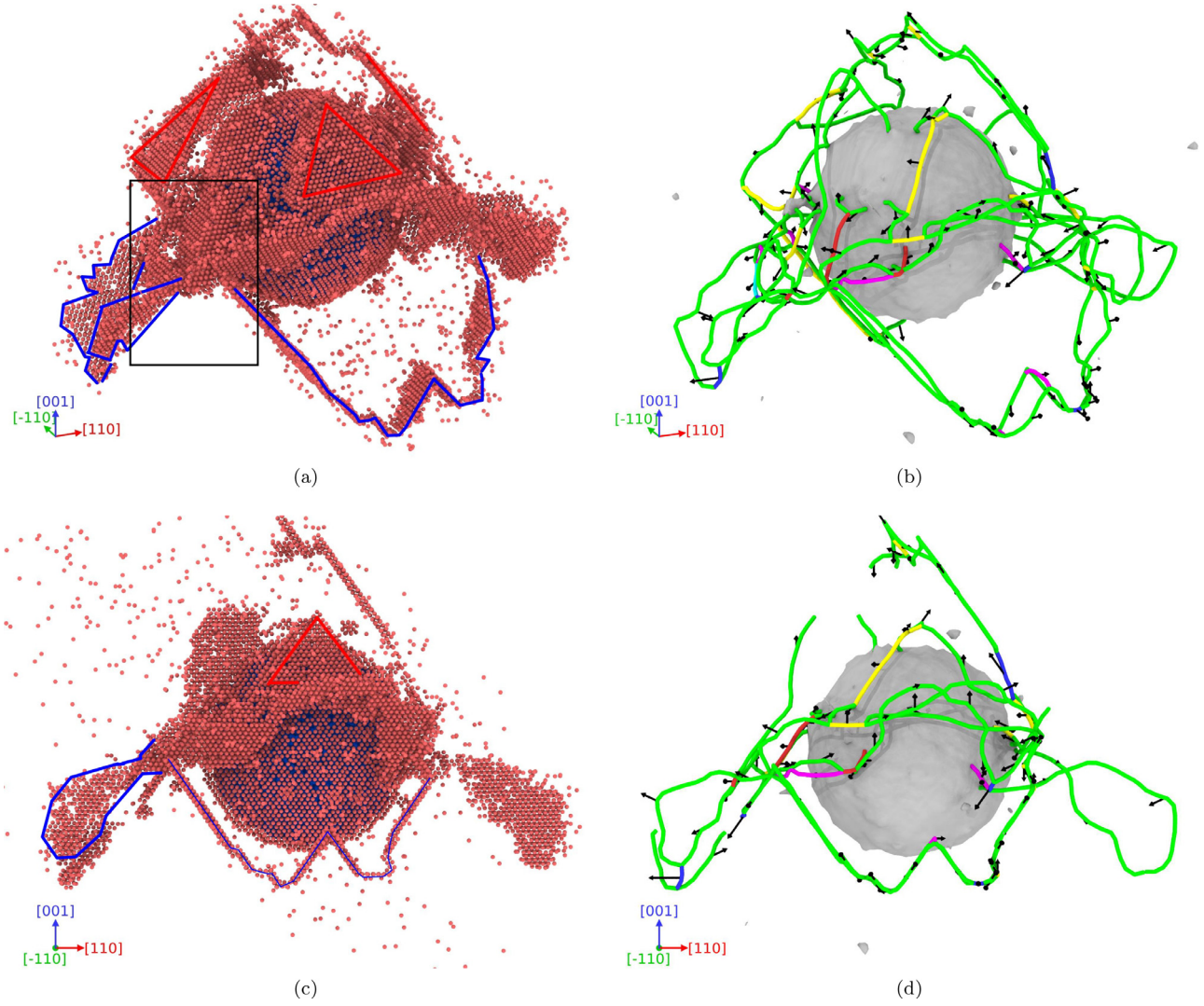

Fig. 7. Final configuration of the bubble with $n_{H/vac} = 3$, (a–d), In the left panel (a,c) only the atoms with CS parameter above 4.5 are shown for clarity. In the right panel (b,d) the dislocation lines identified by DXA [67] are shown in different colors according to the dislocation type. The following colors were used: green for Shockley partials, blue for perfect dislocations, red for "others" dislocations, pink for stair-rod, yellow for Hirth and cyan shows Frank partial dislocations. Burger's vector are shown for clarity. In (c and d), the features on the back were remove for clearer view. (For interpretation of the references to colour in this figure legend, the reader is referred to the web version of this article.)

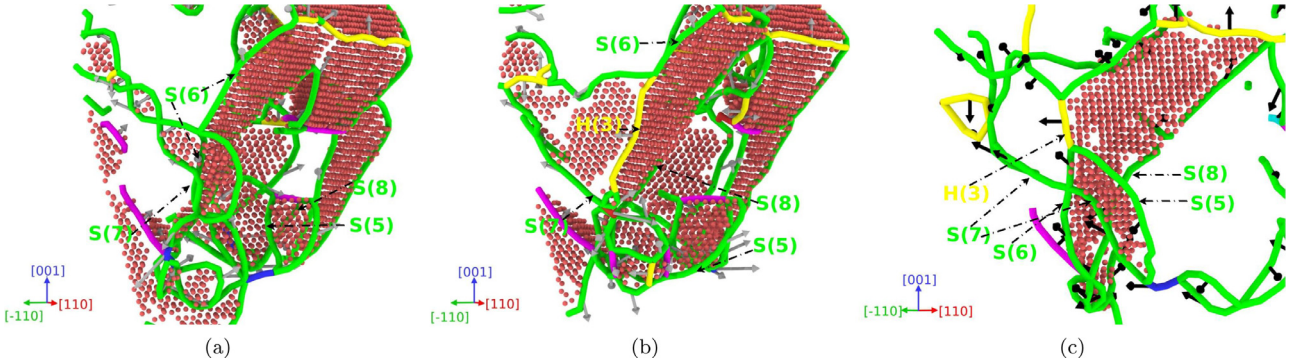

Fig. 8. Configuration of the bubble with $n_{H/vac} = 3$ at (a) 64 ps (b) 66.5 ps and (c) 69 ps (corresponding region marked with a black region in Fig. 7a). The dislocation lines identified by DXA [67] are shown in different colors according to the dislocation type. The HCP atoms contained by them are shown as well for clarity. The following colors were used: green for Shockley partials, blue for perfect dislocations, red for "others" dislocations, pink for stair-rod, yellow for Hirth and cyan shows Frank partial dislocations. Burger's vector are shown for clarity.The Burgers vectors of the dislocations are shown. Inset: the region of analysis is marked in black. We identify the following dislocations: **H(3)** with $\vec{b} = \frac{1}{3}[0\,1\,0]$, **S(5)** with $\vec{b} = \frac{1}{6}[2\,1\,\bar{1}]$, **S(6)** with $\vec{b} = \frac{1}{6}[\bar{2}\,1\,1]$, **S(7)** with $\vec{b} = \frac{1}{6}[1\,2\,1]$ and **S(8)** with $\vec{b} = \frac{1}{6}[\bar{1}\,2\,\bar{1}]$. (For interpretation of the references to colour in this figure legend, the reader is referred to the web version of this article.)

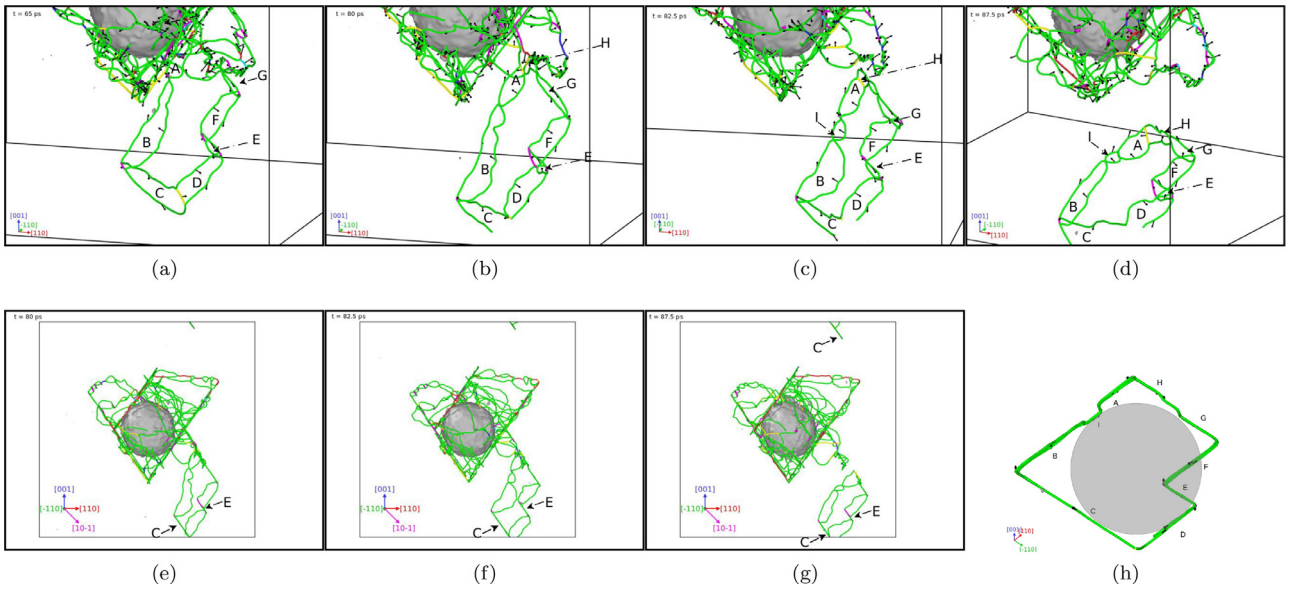

Fig. 9. (a–d) Perspective of evolution of the prismatic loop composed by different shear loops. (e–g) Evolution of the prismatic loop showing that shear loops slip in the same plane since it detaches, while the loop move in the $[1\,0\,\bar{1}]$. (h) Configuration of the detached loop viewed in the direction of movement. Other dislocations which are not part of the loop are removed in the image for clarity. The grey circle is the projection of the void. Green color shows Shockley partials, blue shows perfect, red shows "others" dislocations, pink shows stair-rod, yellow shows Hirth and cyan shows Frank partial dislocations.. (For interpretation of the references to colour in this figure legend, the reader is referred to the web version of this article.)

with the loop of interstitials leaving directly from the surface of the bubble [40,41].

We further analyze the shape of the partial prismatic loop seen in Fig. 7(c,d). Following the dislocation dynamics around the bubble we see that the shear loops are emitted either directly from the surface (see in Fig. 7(c) the lowest shear loops in the shape of the "W" letter) or continued from those sides of the octahedron that are parallel to the same $\langle 1\,1\,0\rangle$ direction (as well as the direction in which the lowest shear loops glide)). Emission directly from the bubble surface is a straight forward process, while extension of the sides of the forming octahedron is less trivial, since the octahedron edges are normally locked by the Hirth locks, see Fig. 6(b).

In Fig. 8 we zoom in the region outlined by a black rectangular in Fig. 7(a) to show the process of Hirth lock dissociation in a greater detail. In Fig. 8 we observe two perfect dislocations composed of Shockley partials marked in the figure as **S(i)**:

$$\mathbf{S(5)}+\mathbf{S(7)}=\frac{a}{6}[2\,1\,\bar{1}]+\frac{a}{6}[1\,2\,1]\longrightarrow\frac{a}{2}[1\,1\,0]$$
$$\mathbf{S(6)}+\mathbf{S(8)}=\frac{a}{6}[\bar{2}\,1\,1]+\frac{a}{6}[\bar{1}\,2\,\bar{1}]\longrightarrow\frac{a}{2}[\bar{1}\,1\,0]$$

These are able to lock in the perfect Hirth lock with $\vec{b}=[0\,1\,0]$, however, in our simulations only the leading partials lock in the partial Hirth lock, see Fig. 8(b):

$$\mathbf{S(5)}+\mathbf{S(6)}=\frac{a}{6}[2\,1\,\bar{1}]+\frac{a}{6}[\bar{2}\,1\,1]\longrightarrow\frac{a}{3}[0\,1\,0]$$

When the trailing partial **S(8)** starts gliding further, it induces the dissociation reaction of the partial Hirth lock:

$$\frac{a}{3}[0\,1\,0]\longrightarrow\frac{a}{6}[2\,1\,\bar{1}]+\frac{a}{6}[\bar{2}\,1\,1]=\mathbf{S(5)}+\mathbf{S(6)}$$

This reaction results in the emission of the almost complete shear loop, led by **S(5)** and completed by **S(7)**. This loop, however, is still attached to the bubble but expands rapidly, joining with the shear loops formed previously at the bottom of the bubble via the cross slips.

In these simulations, we observe only partial formation of the prismatic loop. It will not detach from the bubble until the full loop is complete. It may happen on the later stage of the dislocation network evolution (beyond the time span of the current simulation), if the shear loops in the upper part of the bubble also form. However, we do not see any definite tendency towards it. While not impossible, it may be computationally inefficient to continue the simulations under the same condition for longer time. Instead we performed the simulation of the bubble with yet higher H concentration ($n_{H/vac}=4$).

The dislocation network which formed in the $n_{H/vac}=4$ case is shown in Fig. 5(c,d). Although the emission of dislocations around the bubble in this case is very extensive, the view $[\bar{1}\,1\,0]$ in the lower panels of Fig. 9(e–g) show a clear diamond like shape of the octahedron projection in this direction. The emission of the prismatic loop is seen from one of the lower facets of the stacking fault octahedron. More clearly the shear loops forming the prismatic one are seen in the upper panels of Fig. 9(a–d). In both upper and lower panels we clearly see the formation of a prismatic loop, which is detaching and becomes an independently travelling object at the snapshot shown in Fig. 5(c) and 5(d) (the full process of detachment can be found in the video in Supplementary material: *n4disloc.mp4*). This prismatic loop would, at some point, reach the surface or a grain boundary. As we saw in detail in case of $n_{H/vac}=3$, the formation of the prismatic loop is possible due to communicating shear loops, which can be emitted directly from the bubble surface and from the nodes where several dislocations meet above the bubble surface.

We show the projection of the emitted prismatic loop on the $[1\,0\,\bar{1}]$ direction in Fig. 9(h). Here we see that the punched prismatic loop is surrounded by a number of shear loops. Generally, to enclose a prismatic loop within an FCC lattice, it is sufficient to nucleate four joined shear loops (two on the parallel {111} slip planes with the opposite Burgers vectors and two on the other parallel {111} slip planes tilted with respect to the first ones at 71° of the acute angle). In the final shape of the loop (Fig. 9(c) and 9(d)), we identified 9 different shear loops that are marked by the capital Latin letters from **A** to **I**:

$$\mathbf{A,\,B,\,I:}\frac{1}{2}[\bar{1}\,0\,1]\longrightarrow\frac{1}{6}[\bar{2}\,\bar{1}\,1]+\frac{1}{6}[\bar{1}\,1\,2]$$

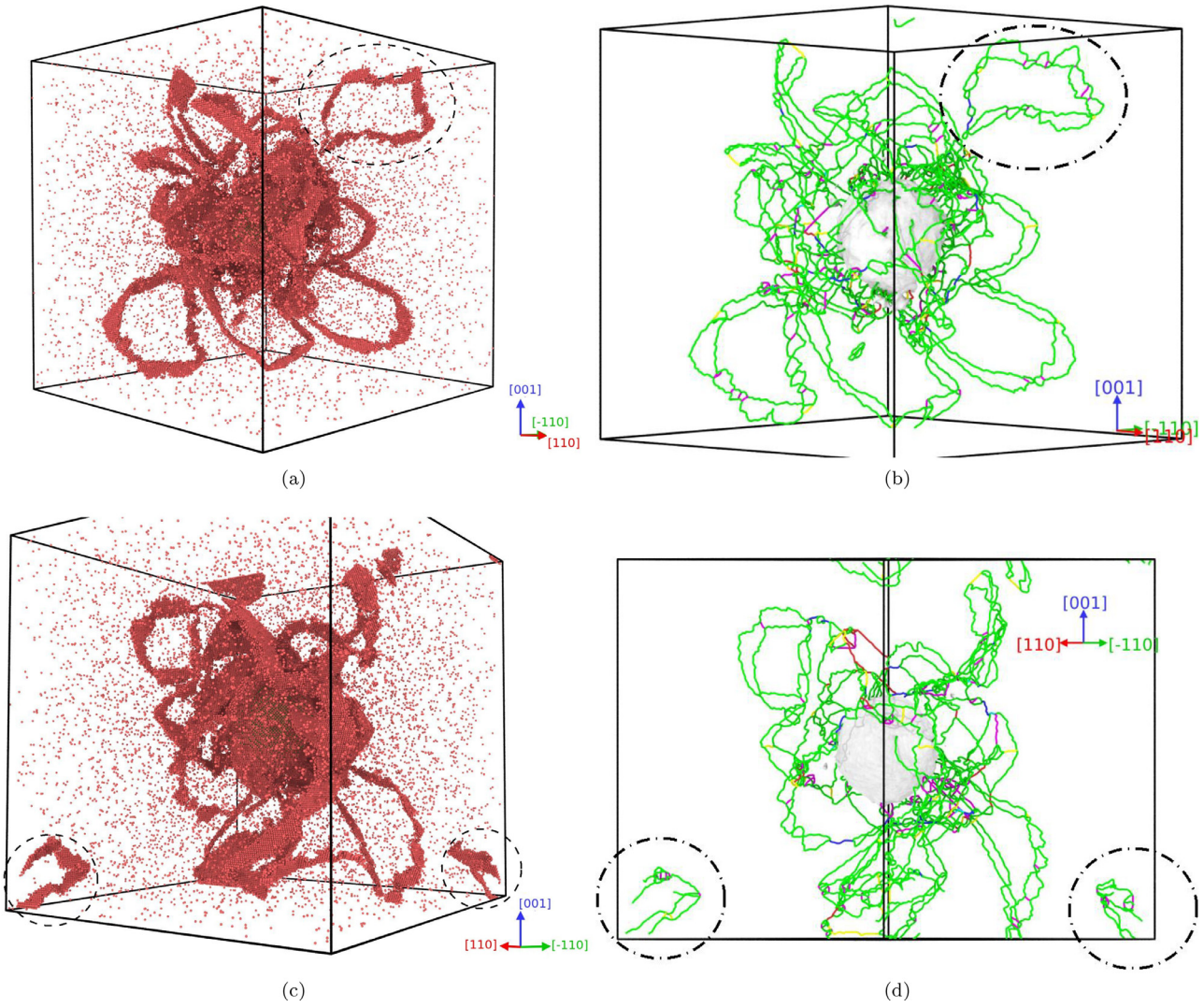

Fig. 10. Evolution of the bulk cell for the concentration of $n_{H/vac} = 5$ at 36 ps ((a),(b)) and at 100 ps ((c),(d)). Only those atoms with CS greater than 4.5 are plotted (a,c) and dislocations in the cell (b,d). Green color shows Shockley partials, blue shows perfect, red shows "others" dislocations, pink shows stair-rod, yellow shows Hirth and cyan shows Frank partial dislocations. Dashed ellipses marked the dislocation loops. (For interpretation of the references to colour in this figure legend, the reader is referred to the web version of this article.)

$$\textbf{C:}\ \frac{1}{2}[1\,0\,\bar{1}] \longrightarrow \frac{1}{6}[2\,\bar{1}\,\bar{1}] + \frac{1}{6}[1\,1\,\bar{2}]$$
$$\textbf{D, F:}\ \frac{1}{2}[1\,0\,\bar{1}] \longrightarrow \frac{1}{6}[2\,1\,\bar{1}] + \frac{1}{6}[1\,\bar{1}\,\bar{2}]$$
$$\textbf{E, G, H:}\ \frac{1}{2}[\bar{1}\,0\,1] \longrightarrow \frac{1}{6}[\bar{2}\,1\,1] + \frac{1}{6}[\bar{1}\,\bar{1}\,2]$$

The prismatic loop started to be completed after the **A** and **G** shear loops commenced to form at 65 ps since the beginning of the simulation (see Fig. 9(a,e)). They gradually grew under the pressure in the bubble and eventually detached from the latter (Fig. 9(b,f)). However, the whole prismatic loop was still attached to the bubble (or rather to the dislocation node near the bubble surface) via the shear loop **H**, which also started growing (see Fig. 9(c)) connecting with the shear loop **A** via the Hirth partial and with the **G** via a cross-slip. Eventually when the **H** shear loop became too large to be maintained attached to the dislocation node under the simulation condition, it also detached and the whole prismatic loop was emitted in the $[1\,0\,\bar{1}]$ after 87.5 ps of the simulated time (Fig. 9(d,g)). We also note that after detachment the shape of the loop did not change.

The view of the prismatic loop in the direction of its motion shows the cross section of the loop in Fig. 9(h), which kept its shape until the end of the simulation (not expanding as suggested in [36]) offering a direct mass transport mechanism. Moreover, the inspection of this image reveals that not all the shear loops are independent. For instance, the shear loops **A** and **B** are separated by the small shear loop **I**, which has formed as a result of a double jog of the shear loop **B** on the parallel slip plane. Similarly the shear loops **H** and **G** are connected via a single jog. However, the shear loops **D** and **F** are clearly separated and most likely were formed independently, but eventually joined via the shear loop **E**. We also see that the Burgers vectors of the shear loops (which correspond to the perfect Shockley dislocations) are either aligned opposite to the gliding direction (loops **A, B, I, E, G** and **H**) or along the gliding direction (loops **C, D** and **F**. This indicates that there is an extra plane perpendicular to the gliding direction and dissociated between the shear loops around it. Emission of a similar prismatic loop was observed also under uniaxial stress [45,47,71], where a similar prismatic loop nucleated directly at the surface of the near-surface void in Cu, under an applied electric field, in accordance with the model suggested by Lubarda et al. [38] with the yield points at 45° to the normal to the open surface. In the current

simulations under hydrostatic stress we see prismatic loops emitting tangentially to the void surface. Moreover, unlike the prismatic loop described in [41] which were dissociated within the same atomic layers enclosed by the shear loops, we clearly see that the shape of the prismatic loop in FCC structure can be fairly arbitrary. Also the face of such a loop is not clearly defined. The interstitial loop (a loop of an extra layer of atoms) can dissociate not only within the same atomic layers, but also stair-like if some of the shear loops are lagging behind the rest (compare the shear loops **C** and **G**). The only requirement of this construction that there is a link between the shear loops which allows for mass conservation within the loop. This particularly important for large bubbles, where the shear loops can grow fairly large and emit at different times. This will result in emission of prismatic loops of different shapes, however, they still contain an extra plane within the loop, which is taken away from the bubble providing the mechanism of the bubble growth.

Furthermore, the dissociated layer of interstitial atoms does not demand that the size of the dissociated prismatic loop is within the cross section of the bubble. As we see in Fig. 9(h), the loop emitted in our simulations is somewhat larger than the cross section of the void. It is, however, does not imply the violation of the mass conservation law, but rather that dissociation of the extra interstitial layer within the 3D prismatic loop can be uneven.

Due to low stacking fault energy in FCC metals, only the shear loops can be mainly seen in the simulations. The shear loops do not become detached as it is practically impossible to close the loop, if the ends of the dislocation are not pinned [37,72]. Despite the claims of void growth via the shear loops [35,36], we see that these offer only small extension of the bubble volume but do not offer a mechanism for continuous growth process. Without detachment of dislocation loops from the surface, there is no mass transport, hence, there is no actual visible growth of the bubble size. Nevertheless, the experimental images show almost a micrometer size blisters, which suggests the continuous growth of hydrogen bubbles in Cu under the prolonged irradiation with the H ions. Comparing the shape of the loop in Fig. 9(g) and the experimental image in Fig. 2 we observe a clear resemblance of the shapes of the loop and the shape of the blister on the surface. Such perfect geometric shape can grow only as a result of plastic deformations, i.e. punching of complete prismatic loops in one of the ⟨1 1 0⟩ directions. Moreover, the same shape of the protrusion we saw in [47] on {1 1 0} Cu surface, which resulted from punched prismatic loops from a near-surface void.

We further observe even more dramatic behavior of the bubble growth with $n_{H/vac} = 5$. Here a dislocation loop, of the similar nature as the one observed in Fig. 9, is emitted from the bubble surface in one of the [1 0 1] directions already after 36 ps (Fig. 10(a) and 10(b)). This prismatic loop appears as an independent object in Fig. 10(c) and 10(d), which has crossed the periodic boundaries and re-appeared in the cell again. In experimental condition, the prismatic loop emitted from the surface of the bubble will glide in the emitted direction until it is absorbed in the grain boundary. We also observe the large number of the shear dislocations which are attached to the bubble. They increase in size, but do not leave the bubble surface and, hence, cannot participate in the mass transport away from the bubble (the whole process can be followed in the movie in Supplementary *n5disloc.mp4*). The higher pressure within the bubble leads to more extensive dislocation network around it, however, the mechanisms of dislocation interactions remain the same (for more information see Supplementary material).

4. Conclusions

In conclusion, we studied the mechanisms of plastic deformation around hydrogen bubbles in Cu to explain the distinct geometric shapes on the bubbles grown on Cu surface under negative H ion irradiation. We performed a number of molecular dynamic simulations of large pre-existing hydrogen bubbles filled with hydrogen gas of different concentrations. In the simulations, we observed only elastic dilation of the bubble when the H concentration inside of it was below two hydrogen atoms per one Cu vacancy. At $n_{H/vac} \approx 2.5$, the stacking faults start growing around the bubble. These can form an almost complete stacking fault octahedron hardening the surface of the bubble. After $n_{H/vac} = 3$, the pressure of H gas is sufficient to emit shear loops on adjacent planes in one of {1 1 0} directions away from the bubble. However, the emission of a full prismatic loop we observe only at $n_{H/vac} = 4$. Surprisingly, the emitted loop can have area larger than the bubble cross section as it continues from the sides of enveloping stacking fault octahedron. This becomes possible only when the pressure within the bubble is sufficient to break through Hirth locks terminating the faces of the octahedron. Moreover, we see that these large prismatic loops follow the diamond shape of the {111} planes geometry, although within this geometry, the shape may be arbitrary. Since the shape of the loops does not change while gliding, the clear geometric shapes of prismatic loops is consistent with geometric shape of blisters seen in experimental images.

The dissociation of the prismatic loop in the gliding direction is also arbitrary and depends on how much some of the shear loops enclosing the emitting prismatic loop lag behind. However, all shear loops are connected either by cross slips or by Hirth partial dislocations. Close comparison of the shapes of the prismatic loop cross section and a blister in experimental image, we conclude that the prismatic loop punching is the only plausible mechanism which can explain the continuous growth of blisters in Cu under prolonged irradiation by hydrogen ions.

Declaration of Competing Interest

The authors declare that they have no known competing financial interests or personal relationships that could have appeared to influence the work reported in this paper.

Acknowledgment

The authors acknowledge gratefully the support from the CERN CLIC K-contract (No. 47207461). Computer time granted by the IT Center for Science – CSC – Finland and the Finnish Grid and Cloud Infrastructure (persistent identifier urn:nbn:fi:research-infras-2016072533) is gratefully acknowledged.

Supplementary material

Supplementary material associated with this article can be found, in the online version, at doi:10.1016/j.actamat.2021.117554.

References

[1] J. Condon, T. Schober, Hydrogen bubbles in metals, J. Nucl. Mater. 207 (1993) 1–24.
[2] X. Bai, A. Voter, R. Hoagland, M. Nastas, B. Uberuaga, Efficient annealing of radiation damage near grain boundaries via interstitial emission, Science 327 (5973) (2010) 1631–1634.
[3] R. Smirnov, S. Krasheninnikov, J. Guterl, Atomistic modeling of growth and coalescence of helium nano-bubblesin tungsten, J. Nucl. Mater. 463 (5973) (2015) 359–362.
[4] L. Yang, F. Gaoc, R. Kurtz, X. Zu, S. Peng, X. Long, X. Zhou, Effects of local structure on helium bubble growth in bulk and at grain boundaries of bcc iron: a molecular dynamics study, Acta Mater. 97 (15) (2015) 86–93.
[5] P. Korzhavyi, R. Sandström, Monovacancy in copper: trapping efficiency for hydrogen and oxygen impurities, Comput. Mater. Sci. 84 (2014) 122–128.
[6] D. Stewart, Y. Osetsky, R. Stoller, Atomistic studies of formation and diffusion of helium clusters and bubbles in BCC iron, J. Nucl. Mater. 417 (1–3) (2011) 1110.

[7] M. Ganchenkova, Y. Yagodzinskyy, V. Borodin, H. Hanninen, Effects of hydrogen and impurities on void nucleation in copper: simulation point of view, Philos. Mag. 94 (2014) 3522–3548.
[8] K.O.E. Henriksson, K. Nordlund, J. Keinonen, Molecular dynamics simulations of helium cluster formation in tungsten, Nucl. Instr. Methods Phys. Res. B 244 (2006) 377–391.
[9] M. Thompson, P. Kluth, R. Doerner, N. Kirby, C. Corr, Probing helium nano-bubble formation in tungsten with grazing incidence small angle x-ray scattering, Nucl. Fusion 55 (2015) 042001.
[10] W. Wang, J. Roth, S. Lindig, C.H. Wu, Blister formation of tungsten due to ion bombardment, J. Nucl. Mater. 299 (2001) 124.
[11] F.I. Allen, P. Hosemann, M. Balooch, Key mechanistic features of swelling and blistering of helium-ion-irradiated tungsten, Scr. Mater. 178 (2020) 256–260.
[12] P.B. Johnson, D.J. Mazey, The depth distribution of bubbles and fracture in He^+ and D^+ irradiated copper, J. Nucl. Mater. 111 & 112 (1982) 681–686.
[13] S. Nakahara, Y. Okinaka, Defects induced in copper by cathodic charging of hydrogen, J. Electrochem. Soc. 136 (1989) 1892.
[14] S. Taskaev, D. Kasatov, A. Makarov, I. Shchudlo, In situ observations of blistering of a metal irradiated with 2 Mev protons, in: Proceedings of the IPAC2018, Vancouver, 2018.
[15] R.A. Causey, T.J. Venhaus, The use of tungsten in fusion reactors: a review of the hydrogen retention and migration properties, Phys. Scr. 2001 (2001) T94.
[16] W. Pesch, T. Schober, H. Wenzl, Hydrogen bubble formation by pulse heating in vanadium-hydrogen alloys, Metall. Trans. A 11 (1980) 1821.
[17] T. Schober, H. Conrads, A. Schulz, On the interaction of niobium deuteride with plasmas, Fusion Technol. 23 (1993) 227.
[18] C. Ju, J. Rigsbee, The role of microstructure for hydrogen-induced blistering and stepwise cracking in a plain medium carbon steel, Mater. Sci. Eng. 74 (1985) 47.
[19] M. Iino, The extension of hydrogen blister-crack array in linepipe steels, Metall. Trans. A 9 (1978) 1581.
[20] K. Ravi, V. Ramaswamy, T. Namboodhiri, Hydrogen sulphide resistance of high sulphur microalloyed steels, Mater. Sci. Eng. A129 (1990) 87.
[21] J.-L. Lee, J.Y. Lee, The effect of lattice defects induced by cathodic hydrogen charging on the apparent diffusivity of hydrogen in pure iron, J. Mater. Sci. 22 (1987) 3939.
[22] J.-Y. Lee, J.L. Lee, Hydrogen trapping during cathodic charging of iron, Phys. Chem. NF 146 (1985) 233.
[23] J.-L. Lee, J.Y. Lee, Hydrogen retrapping after thermal charging of hydrogen in iron single crystal, Metall. Trans. A 20 (1989) 1793.
[24] K. Kamada, A. Sagara, H. Kinoshita, Difficulty of dislocation-punching from densely distributed high pressure bubbles, Radiat. Eff. 106 (3) (1988) 219–227.
[25] K. Kamada, Hydrogen implantation effects in the subsurface layer of aluminum - bubble pressure and surface modifications, J. Nucl. Mater. 169 (1989) 141–150.
[26] L. Milacek, R. Daniels, Orientation dependence of pitting and blistering in proton-irradiated aluminum crystals, J. Appl. Phys. 39 (1968) 5714.
[27] L. Milacek, R. Daniels, Proton-radiation-induced blistering of aluminum, J. Appl. Phys. 39 (1968) 2803.
[28] R. Daniels, Correlation of hydrogen evolution with surface blistering in proton-irradiated aluminum, J. Appl. Phys. 39 (1971) 417.
[29] M. Sznajder, U. Geppert, M. Dudek, Hydrogen blistering under extreme radiation conditions, npj Mater. Degrad. 2 (2018) 1.
[30] S. Nakahara, Y. Okinaka, Microstructure and mechanical properties of electroless copper deposits, Ann. Rev. Mater. Sci. 21 (1991) 93.
[31] M. Fukui, R. Sakamoto, K. Araki, T. Fujiwara, T. Muroga, N. Yoshida, In situ observation of low energy hydrogen ion irradiation damage in copper, J. Nucl. Mater. 220–222 (1995) 810–814.
[32] A. Robinson, P. Edmondson, C. English, S. Lozano-Perez, G. Greaves, J. Hinks, S. Donnelly, C. Grovenor, The effect of temperature on bubble lattice formation in copper under in situ He ion irradiation, Acta Mater. 131 (2017) 08–111.
[33] P. Johnson, D. Mazey, Hydrogen gas-bubble structure in Cu, J. Nucl. Mater. 91 (1980) 41–46.
[34] F. Granberg, X. Wang, D. Chen, K. Jin, Y. Wang, H. Bei, W. Weber, Y. Zhang, K. More, K. Nordlund, F. Djurabekova, Origin of increased helium density inside bubbles in $Ni(1-x)Fe_x$ alloys, Scr. Mater. 191 (2021) 1–6.
[35] S. Traiviratana, E. Bringa, D. Benson, M. Meyers, Void growth in metals: atomistic calculations, Scr. Mater. 56 (2008) 3874–3886.
[36] Y. Cui, Z. Chen, Material transport via the emission of shear loops during void growth: a molecular dynamics study, J. Appl. Phys. 119 (2016).
[37] V.V. Bulatov, W.G. Wolfer, M. Kumar, Shear impossibility: comments on “void growth by dislocation emission” and “void growth in metals: atomistic calculations”, Scr. Mater. 63 (1) (2010) 144–147.
[38] V. Lubarda, M. Schneider, D. Kalantar, B. Remington, M. Meyersa, Void growth by dislocation emission, Acta Mater. 52 (6) (2004) 1397–1408.
[39] D.C. Ahn, P. Sofronis, M. Kumar, J. Belak, R. Minich, Void growth by dislocation-loop emission, J. Appl. Phys. 101 (2007) 063514.
[40] H. Xie, N. Gao, K. Xu, G.-H. Lu, T. Yu, F. Yin, A new loop-punching mechanism for helium bubble growth in tungsten, Acta Mater. 141 (2017) 10–17.
[41] M. Jin, Y. Gao, Y. Zhang, C. Jiang, J. Gan, Dissociated prismatic loop punching by bubble growth in fcc metals, Sci. Rep. 11 (2021) 12839.
[42] J. Marian, B.D. Wirth, J.M. Perlado, Mechanism of formation and growth of $< 100 >$ interstitial loops in ferritic materials, Phys. Rev. Lett. 88 (2002) 255507.
[43] X.H. Long, D. Wang, W. Setyawan, P. Liu, N. Gao, R.J. Kurtz, Z.G. Wang, X.L. Wang, Atomistic simulation of interstitial dislocation loop evolution under applied stresses in BCC iron, Phys. Status Solidi (a) 215 (1) (2018) 1700494.
[44] N. Zhou, K.I. Elkhodary, X. Huang, S. Tang, Y. Li, Dislocation structure and dynamics govern pop-in modes of nanoindentation on single-crystal metals, Philos. Mag. 100 (2020) 12.
[45] A.S. Pohjonen, F. Djurabekova, A. Kuronen, S.G. Fitzgerald, K. Nordlund, Analytical model of dislocation nucleation on a near-surface void under tensile surface stress, Philos. Mag. 92 (2012) 1–17.
[46] A. Pohjonen, F. Djurabekova, A. Kuronen, K. Nordlund, MD simulations of near surface void in copper under thermal compression, in: Proceedings of the MRS Symposium Proceedings, Warrendale, PA, USA: MRS, 2011.
[47] A.S. Pohjonen, S. Parviainen, T. Muranaka, F. Djurabekova, Dislocation nucleation on a near surface void leading to surface protrusion growth under an external electric field, J. Appl. Phys. 114 (2013) 033519.
[48] S. Sgobba, F. Leaux, in: Spec. No. 2001_Cu-OFE_bars-blanks-ingots, EDMS, CERN, Geneva, 2017.
[49] A. Saressalo, A. Kyritsakis, F. Djurabekova, I. Profatilova, J. Paszkiewicz, S. Calatroni, W. Wuensch, Classification of vacuum arc breakdowns in a pulsed dc system, Phys. Rev. Accel. Beams 23 (2020) 023101.
[50] M. Calviani, Private Communication, in: CERN,
[51] K. Nordlund, J. Keinonen, E. Rauhala, T. Ahlgren, Range profile in self-ion-implanted crystalline Si, Phys. Rev. B 52 (1995) 15170.
[52] Y. Mishin, M. Mehl, D. Papaconstantopoulos, A. Voter, J. Kress, Structural stability and lattice defects in copper: Ab initio, tight-binding, and embedded-atom calculations, Phys. Rev. B 63 (22) (2001).
[53] S. Foiles, M. Baskes, C. Melius, M. Daw, Calculation of hydrogen dissociation pathways in nickel using the embedded atom method, J. Less-Common Met. 130 (1987) 465–473.
[54] M.I. Baskes, S. Foiles, C. Melius, Dynamical calculation of low hydrogen reemission off hydrogen covered surfaces, J. Nucl. Mater. 145–147 (1987) 339–343.
[55] J.E. Angelo, N.R. Moody, M.I. Baskes, Trapping of hydrogen to lattice defects in nickel, Model. Simul. Mater. Sci. Eng. 3 (1995) 289–307.
[56] J.F. Ziegler, J.P. Biersack, U. Littmark, The Stopping and Range of Ions in Matter, Pergamon, New York, 1985.
[57] E. Fromm, W. Hehn, G. Hörz, H. Jehn, Gases and carbon in metals, Physics data, Eggenstein-Leopoldshafen, Karlsruhe Fachinformationszent. Kernforsch. Zentralstelle At. Energ., 1984.
[58] X. Zhou, D. Ward, M. Foster, J. Zimmerman, An analytical bond-order potential for the copper–hydrogen binary system, J. Mater. Sci. 50 (2015) 2859–2875.
[59] H.J.C. Berendsen, J.P.M. Postma, W.F. van Gunsteren, A. DiNola, J.R. Haak, Molecular dynamics with coupling to external bath, J. Chem. Phys. 81 (8) (1984) 3684.
[60] J. Li, The mechanics and physics of defect nucleation, MRS Bull. 32 (2007) 151–159.
[61] T. Zhu, J. Li, A. Samanta, A. Leach, K. Gall, Temperature and strain-rate dependence of surface dislocation nucleation, Phys. Rev. Lett. 100 (2008) 025502.
[62] K. Kumar, H. Van Swygenhoven, S. Suresh, Mechanical behavior of nanocrystalline metals and alloys: the golden jubilee issue-selected topics in materials science and engineering: past, present and future, edited by s. suresh, Acta Mater. 51 (19) (2003) 5743–5774. The Golden Jubilee Issue. Selected topics in Materials Science and Engineering: Past, Present and Future
[63] L. Lu, X. Chen, X. Huang, K. Lu, Revealing the maximum strength in nanotwinned copper, Science 323 (5914) (2009) 607–610.
[64] X. Gua, J. Greer, Ultra-strong architected Cu meso-lattices, Extreme Mech. Lett. 39 (2015) 1.
[65] A. Stukowski, Visualization and analysis of atomistic simulation data with ovito – the open visualization tool, Model. Simul. Mater. Sci. Eng. 18 (2010) 015012.
[66] C.L. Kelchner, S.J. Plimpton, J.C. Hamilton, Dislocation nucleation and defect structure during surface indentation, Phys. Rev. B 58 (1998) 11085.
[67] A. Stukowski, V. Bulatov, A. Arsenlis, Automated identification and indexing of dislocations in crystal interfaces, Model. Simul. Mater. Sci. Eng. 20 (2012) 085007.
[68] A. Stukowski, Computational analysis methods in atomistic modeling of crystals, JOM 66 (2014) 399–407.
[69] T. Paulauskas, C. Buurma, E. Colegrove, B. Stafford, Z. Guo, M.K.Y. Chan, C. Sun, M.J. Kim, S. Sivananthan, R.F. Klie, Atomic scale study of polar Lomer–Cottrell and Hirth lock dislocation cores in CdTe, Acta Crystallogr. Sect. A A70 (2014) 524–531.
[70] D.K. Mishra, M. Meraj, S.K. BadJena, S. Pal, Dislocation interaction and V-shaped growth of the distorted structure during nanoindentation of $Cu_20Ni_20Al_20Co_20Fe_20$ (high-entropy alloy)-coated copper: A molecular dynamics simulation-based study, Trans. Indian Inst. Met. 72 (2019) 167–180.
[71] A.S. Pohjonen, F. Djurabekova, A. Kuronen, K. Nordlund, S. Fitzgerald, Dislocation nucleation from near surface void under static tensile stress on surface in Cu, J. Appl. Phys. 110 (2011) 023509.
[72] H. Sui, L. Yu, W. Liu, L. Chen, H. Duan, Three dimensional dislocation-loop emission criterion for void growth of ductile metals, Int. J. Plast. 131 (2020) 102746.